Article Supplement

Spatial variability in winter mass balance on Storglaciären modelled with a terrain based approach.

Y. Terleth, W.J.J. Van Pelt, R. Pettersson

Code Availability

A Matlab version of the ST-EBFM model is available at https://github.com/yoramterleth/ST-EBFM.

S.1: Spatial & Temporal Variability of Winter Balance on Storglaciären

Here we present a brief investigation of the spatial and temporal variability within the accumulation patterns observed on Storglaciären, in an effort to provide context for our model results. Figure 1 is a winter balance focused reiteration of Figure 2 in Jansson & Pettersson (2007). It shows the very high accumulation values observed at location A, likely exposed to snow avalanches originating in the steep headwall of Kebnekaise. Location B is characterised by near average winter balance. Jansson & Pettersson (2007) suggest that the low accumulation in values in location C are caused by wind driven snow erosion.

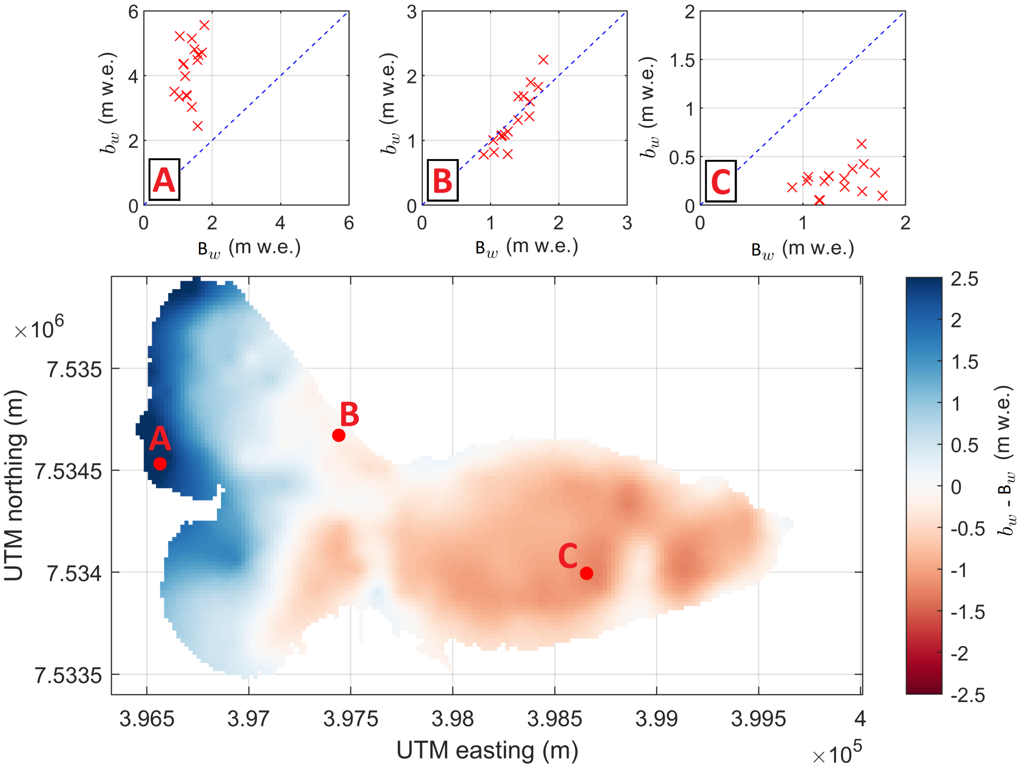

Figure 1: Methodology following Jansson & Pettersson (2007). Yearly glacier wide B_w subtracted from yearly specific b_w, averaged over the 1995-2010 accumulation seasons. Scatter-plots show values for location **A** likely affected by avalanching, **B** unaffected by snow transport processes and close to the E.L.A. and **C** affected by wind driven erosion of deposited snow.

Since terrain remains virtually unchanged at the considered timescale, variability in accumulation is likely to be relatively constant in location and extent from year to year. A similar suggestion is made in McGrath et al. (2018), where accumulation patterns are found to be consistent over time. We borrow the methodology for evaluating inter-annual variability in accumulation from McGrath et al. (2018) in the present work: Figure 2 **A** shows the normalized range in winter balance and Figure 2 **B** shows the coefficient of determination. There is strong year to year variability especially in areas that were concluded to be affected by wind erosion by Jansson & Pettersson (2007); but it seems likely that this is at least in part a feature of the extremely low b_w values as Figure 2 **A** shows the lowest absolute normalised range in the same area. As such, the absolute variability of wind driven accumulation is quite low, suggesting terrain plays a strong role in snow redistribution by wind; this is in line with results presented in McGrath et al. (2018). Meanwhile, areas of low R^2 and high absolute range just below the western headwall are likely affected by gravitational snow transport. Sloughing and avalanching, while facilitated by topography, are the consequence of a sequence of meteorological events that shape snow conditions in the initiation zone (e.g. Schweizer et al. 2003). It seems plausible that the notoriously erratic and difficult to predict events would occur less reliably from year to year, and thus produce the high normalized range values and low R^2 values in the upper accumulation zone. This short analysis of inter-annual variability strengthens the suspicion that Storglaciären's winter balance is influenced by post-depositional mass redistribution, with the 350% range in Figure 2 **A** hinting at considerable but temporally variable impacts from avalanching.

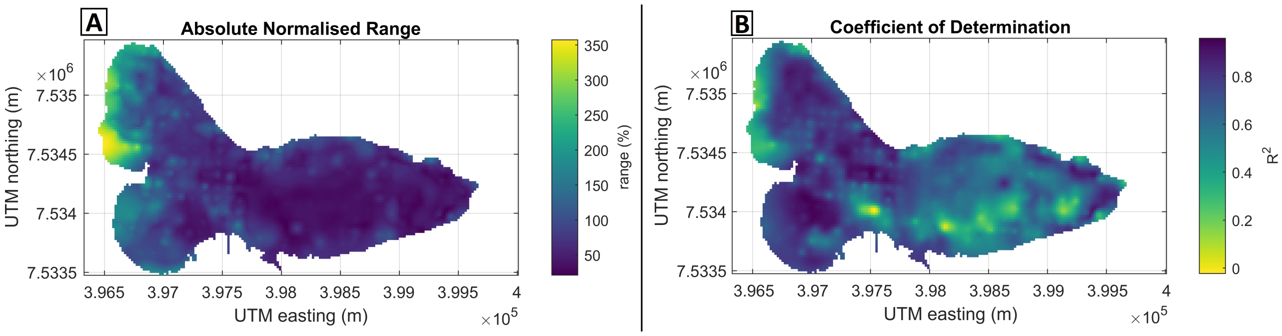

Figure 2: Methodology following McGrath et al. (2018). Interannual variability of b_w from 1995-2010. Quantified via: **A** absolute normalized range: b_w is divided by B_w, the range is then the smallest yearly value subtracted from the largest yearly value. The method gives a good indication of the areas with largest variability, but is sensitive to outliers. **B** Coefficient of determination R^2 between the b_w and B_w. The method is more robust to outliers but is less suitable in areas where b_w trends towards zero.

S.2: Comparison of precipitation records

Here we show a brief comparison of precipitation records measured at the Tarfala AWS, the Nikkaluokta AWS, and the Kråkmo AWS, located on the west side of the Scandes range on the Norwegian coast and notably used to estimate snowfall on Storglaciären in Evans et al. (2008). We conduct the comparison for the sporadic time periods for which measurements from the Tarfala weather station are available, primarily during the summer and fall (Fig.3. It should be noted that while this comparison provides hints towards whether weather stations can be considered indicative of precipitation values in the Tarfala valley, they are not conclusive due to the relatively limited temporal extent of the comparison. Precipitation patterns in the region tend to undergo seasonal variations (Jansson et al. 2007), and thus the observed similarities and differences should be treated with care.

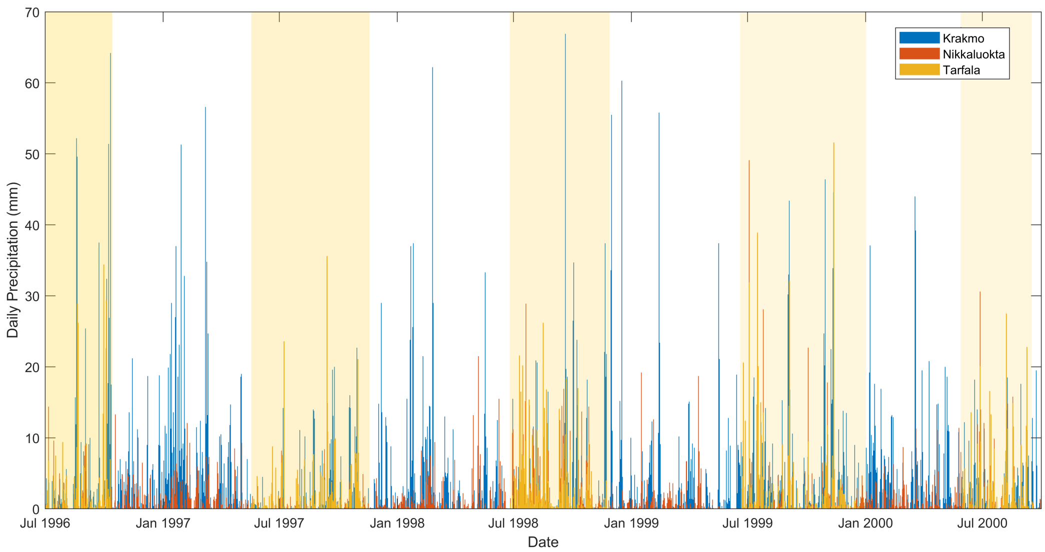

Figure 3: Time series of daily precipitation totals recorded at automatic weather stations at Tarfala and Nikkaluokta, obtained through SMHI, and at Kråkmo, obtained through the European Climate Assesment Database. Comparisons in subsequent figure are conducted for the highlighted periods, during which all three records are available.

Figure 4 shows scatter plots comparing daily precipitation between Tarfala and Nikkaluokta, and between Tarfala and Kråkmo. The closer the data plot to the 1:1 line, the better the correlation between observed precipitation at both locations.

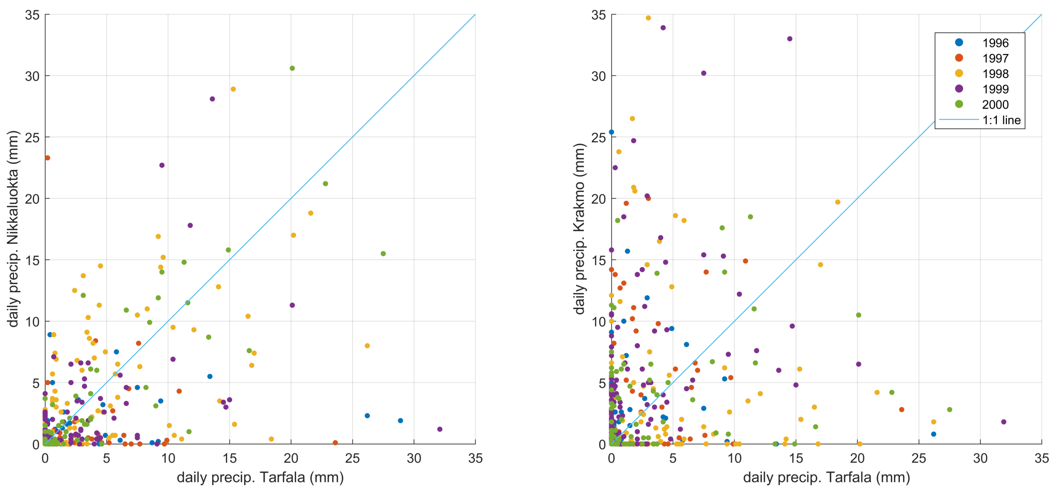

Figure 4: Scatter plots of daily precipitation totals recorded at automatic weather stations at Tarfala and Nikkaluokta, and at Tarfala and Kråkmo. 1:1 line indicates a perfect correlation between the stations.

Table 1 shows the correlation coefficients between the observed daily values at the Tarfala AWS and at both of the compared stations. Over the compared intervals, we generally find better agreement between Tarfala and the Nikkaluokta AWS. Thus we view the Nikkaluokta record as most indicative of precipitation in the Tarfala valley, and elect to use these data, as model input. Fitting a trend-line to the values observed at Tarfala and at Nikkaluokta yields a slope of 1.33, which motivates the linear correction of 133% we apply to precipitation measurements at Nikkaluokta, and which we suggest is as representative as possible of conditions at Tarfala. Figure 5 shows a comparison of the cumulative precipitation estimated with this 133% gradient and the observed precipitation at the Tarfala AWS over the summer and fall of 1999. Nevertheless, the usage of precipitation data from a distant source remains a source of error and uncertainty within our model.

Table 1: Correlation coefficients between daily precipitation at Tarfala and at Nikkaluokta, and between daily precipitation at Tarfala and at Kråkmo, over each of the comparison periods.

Period	Tarfala AWS and Nikkaluokta AWS correlation coefficient in daily precipitation	Tarfala AWS and Kråkmo AWS correlation coefficient in daily precipitation
1996/07/15 - 1996/09/30	0.3320	0.4775
1997/06/30 - 1997/10/01	0.3843	0.1257
1998/07/01 - 1998/11/01	0.5968	0.1562
1999/07/01 - 1999/12/01	0.5938	0.5573
2000/06/15 - 2000/09/15	0.8565	0.3006

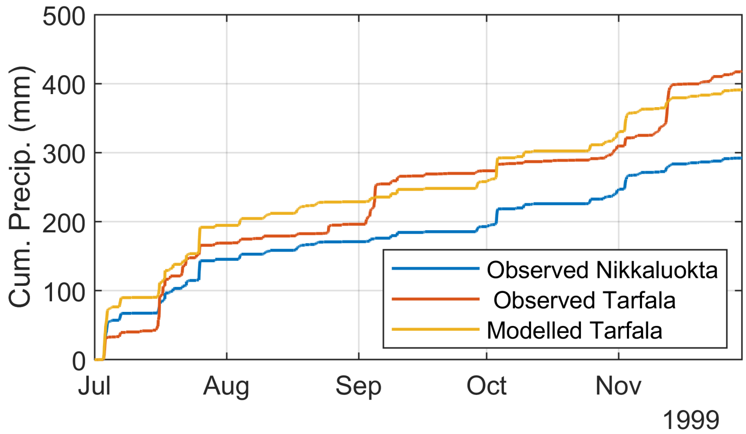

Figure 5: Comparative example of cumulative precipitation July 1st 1999 to November 30th 1999. Values observed at Tarfala AWS and at Nikkaluokta AWS. The yellow line shows values for Tarfala used as model input, estimated as 133% of the values recorded at Nikkaluokta.

S.3: Comparison of Calibration and Validation Period Winter Climates

Figure 6 shows average monthly cumulative precipitation, mean temperature, and wind speed and directions for the calibration period (1997-2003 winters) and the validation period (2004-2010 winters). We note differences for certain specific months between the two period, but these seem driven by outliers. The overall winter precipitation, temperature and wind speed and direction are relatively uniform between the two periods.

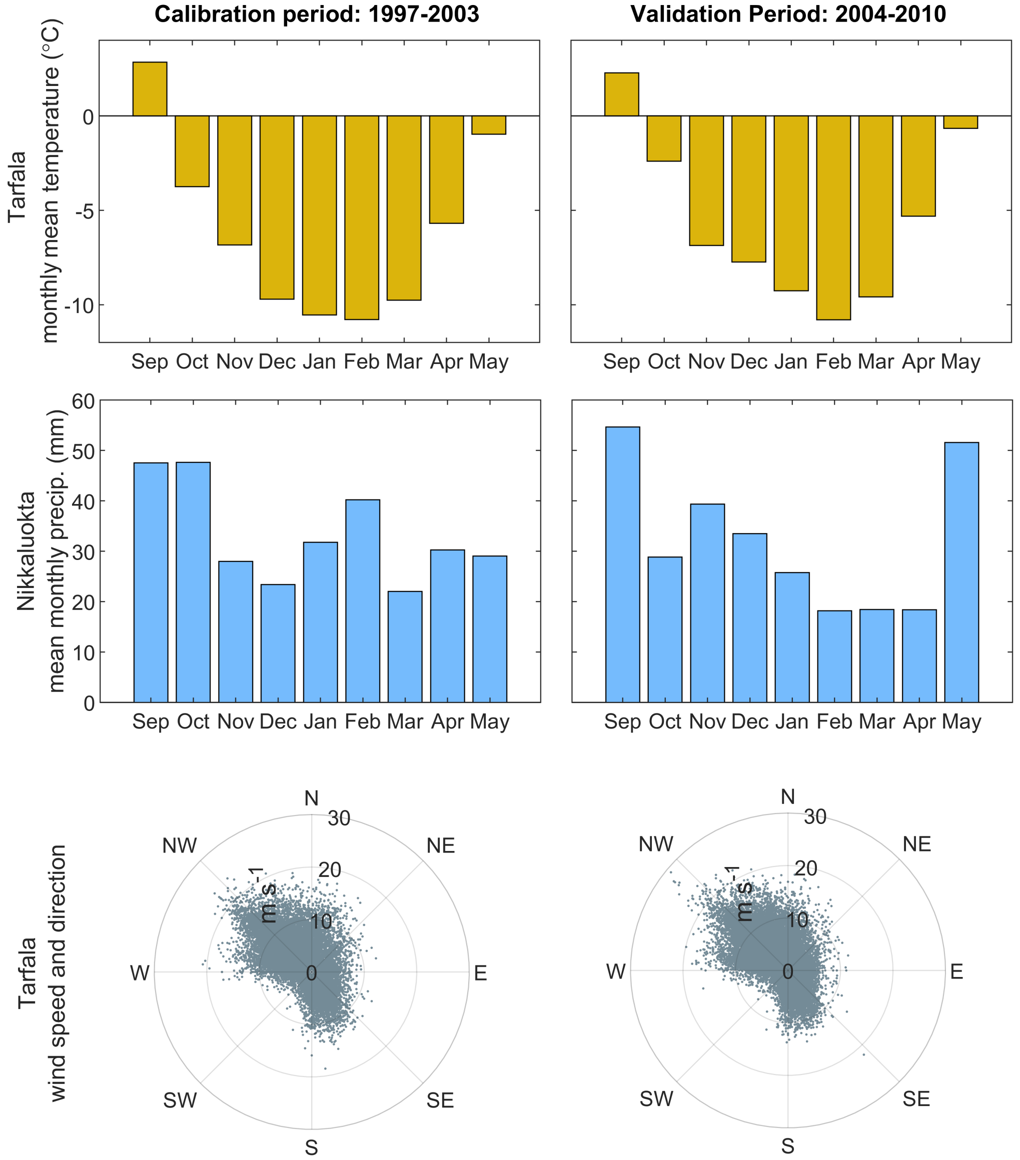

Figure 6: Comparison of average monthly cumulative precipitation, mean temperature, and wind speed and directions for the 1997-2003 and 2004-2010 winters

S.4: Wind Driven Snow Transport Model Description

The modelling approach described in Winstral et al. (2002) initially determines a sheltering factor for each cell of a Digital Elevation Model. This sheltering factor is specific to a prevailing wind direction, and is computed in this application for sixteen wind directions at 22.5° intervals. For each direction and each cell, a ”slice” of 30° wide is considered through seven vectors spaced by 5° and of a length SD_{max}, the maximum distance at which terrain would affect snow deposition (Fig. 7) In this study, SD_{max} is used as a calibration parameter and varied between 100 m and 1000 m.

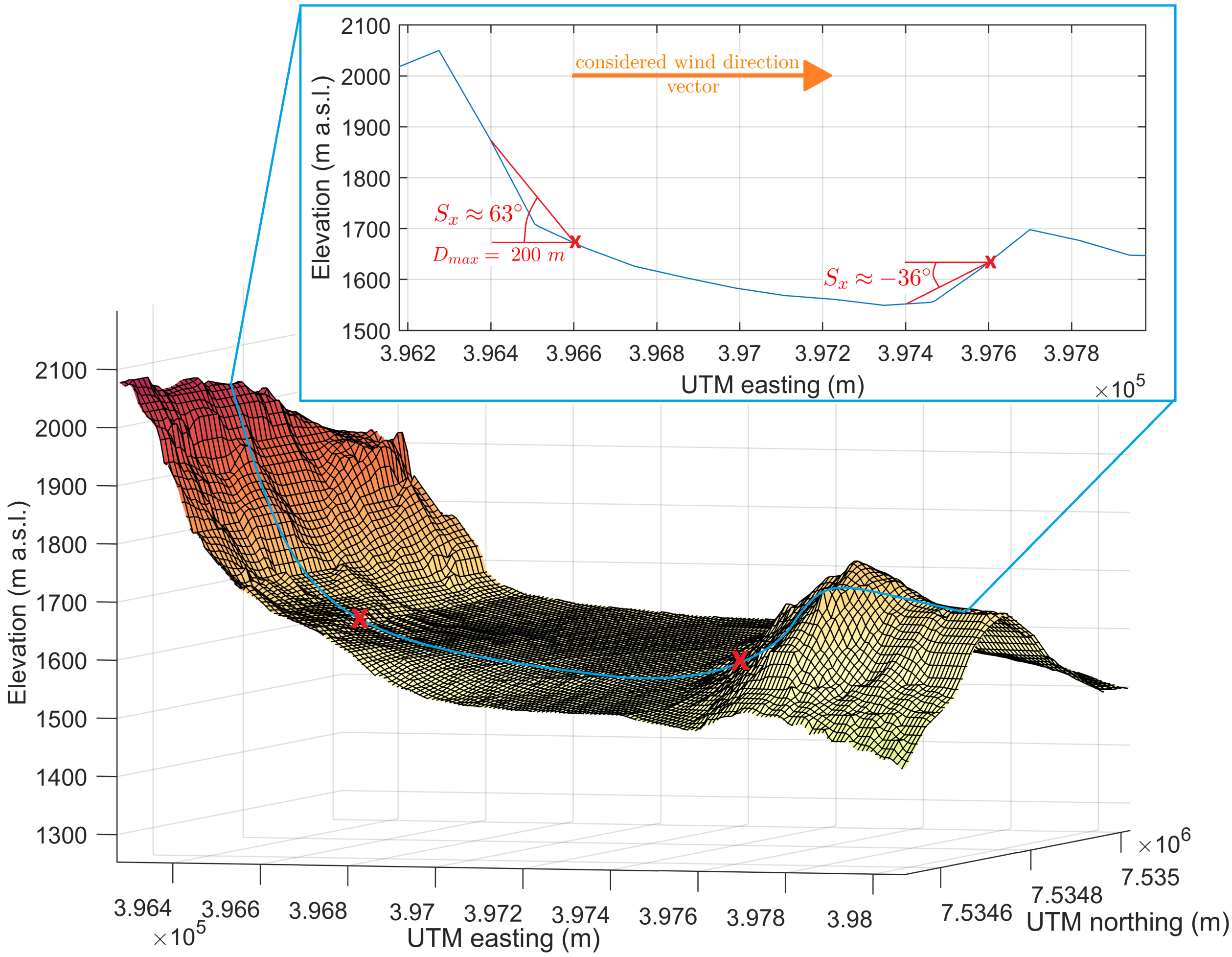

Figure 7: **based on Winstral et al. (2002).** Along each considered wind direction vector, the S_x for each cell corresponds to the maximum angle to upwind terrain within the search distance SD_{max}. In this example, SD_{max} = 200 m and the direction of the considered wind vector direction v is west (270°).

For any upwind vector v and for any cell (x_i,y_i) with an elevation Z, the maximum angle S_x to an upwind cell (x_v,y_v) along v within the search distance D_{max} is determined following Winstral et al. (2002):

$$S_x(x_i, y_i) = \max\left[\tan\left(\frac{Z(x_v, y_v) - Z(x_i, y_i)}{\sqrt{(x_v - x_i)^2 + (y_v - yi)^2}}\right)\right] \tag{1}$$

A higher S_x indicates the upwind presence of nearby and prominent relief, conditions favorable for deposition. Meanwhile, negative S_x values point to lower elevations upwind of the considered cell, indicating the location is likely subject to snow erosion (Fig. 7). Since multiple vectors are considered for each "slice" around a prevailing wind direction, equation 1 will yield several S_x values for each cell. The average sheltering index $\overline{S_x}$ between the vectors A_1 and A_2 at the edges of the "slice", and with a number n_v of increment vectors, follows:

$$\overline{S_x}(x_i, y_i) = \frac{1}{n_v}\sum_{A_1}^{A_2} S_{x_A}(x_i, y_i) \tag{2}$$

The obtained index $\overline{S_x}$ is re-scaled to a [0,1] interval and used as a parameter in the spatial distribution of the precipitation input in the snow model.

As in Winstral et al. (2002), the sheltering index is complemented by the delimitation of drift zones in the lee of slope breaks, sudden changes in slope angle that indicate a ridge perpendicular to the slope direction at which flow separation is likely to occur. Slope breaks are identified by computing an independent sheltering indices for nearby and faraway terrain. Separation between these two components is set at 75 metres beyond the maximum sheltering distance. The inner zone is then defined between 0 and $SD_{max} + 75$ m upwind from the cell of interest (x_i,y_i) while the outer zone is defined as ranging between SD_{max} + 75 m and SD_{max} + 1000 m. If for the cell of interest the independent sheltering indices for the inner zone and each incremental vector are $S_{inner,\ A}$ and for the outer zone are $S_{outer,\ A}$ (as calculated with equation 1), the average slope break index $\overline{S_b}$ follows Winstral et al. (2002):

$$\overline{S_b}(x_i, y_i) = \frac{1}{n_v} \sum_{A_1}^{A_2} [S_{inner_A}(x_i, y_i) - S_{outer_A}(x_i, y_i)] \tag{3}$$

The $\overline{S_b}$ parameter can be used in combination with $\overline{S_{outer_A}}$ to define the boundaries of a drift zone in which snow deposition will occur. Building on previous field studies and model validation, Winstral et al. (2002) here propose that the minimum average separation angle at the ridge ($\overline{S_b}$) should be larger than 7°. In addition, the exposure of the terrain upwind of the slope break needs ($\overline{S_{outer_A}}$) to be below 5°. These parameters are followed in the current application, and the drift zone selection parameter thus follows:

$$DD(x_i, y_i) = \begin{cases} 1 & \texttt{if } \overline{S_b}(x_i, y_i) > 7^\circ \ \texttt{\&} \ \overline{S_{outer_A}}(x_i, y_i) < 5^\circ \\ 0 & \texttt{otherwise} \end{cases} \tag{4}$$

In Winstral et al. (2002), areas affected by wind sheltering are restricted in space by multiplying the sheltering index $\overline{S_x}$ with DD. This simulates primarily large scale snow drift effects, as represented by the maximum sheltering distances above 100 metres. These effects have been deemed important on Storglaciären, but much smaller scale effects of drifting snow have been explicitly linked to the irregular accumulation pattern (Jansson & Pettersson 2007). Aided by the availability of high resolution topographical information, this study considers a second sheltering index focusing on snow drift at resolutions between 10 and 20 metres. This second sheltering index, S_{xMICRO} is computed following equations 1 and 2. The maximum sheltering distance here is set to 15 metres, as to consider only the elevation difference with the adjacent cells. This type of small scale snow drifting can occur in different settings, such as cross slope where it is not necessarily linked to a ridge or sudden change in terrain angle (McClung & Schaerer 2006). Because of this, the slope break parameters are left out of consideration for the micro scale wind redistribution index. Since $\overline{S_{xMICRO}}$ is not restricted to sheltered areas, negative values can occur, and $\overline{S_{xMICRO}}$ is re-scaled to a [-1,0] interval when negative and a [0,1] interval when positive. Simulating erosion with the sheltering index approach is untested, but the spatial pattern generated seems plausible (Fig. 8). The tolerance of negative values can lead to the total deposited mass differing from the total precipitation, but this also reflects reality rather well as snow could be removed entirely from the glacier surface, just as the large scale $\overline{S_x}$ allows for transport from surrounding terrain onto the glacier surface. It should be noted here that the snow & firn model component undergoes a slight modification to constrain erosion: the mass change resulting from negative wind driven accumulation is valid only if the surface density in below 500 kg m^{-1}, in order to prevent unrealistic situations where ice, firn and avalanche deposits are removed from the surface by wind.

A third parameter P_s preserves the elevation driven spatial precipitation variability. P_s is the $[0, 1]$ re-scaled precipitation at any cell:

$$P_s(x_i, y_i) = P(x_i, y_i) - \frac{\min(P)}{\max(P) - \min(P)} \tag{5}$$

The three obtained parameters of spatial variability in snow deposition are now the "original" spatial variability in precipitation P_s, the micro scale wind redistribution parameter $\overline{S_{xMICRO}}$, and the large scale wind redistribution parameter bound spatially to slope breaks $\overline{S_x} \times DD$. These three parameters, all varying between 0 and 1, are summed into an accumulation factor A_f (Fig. 8):

$$A_f = P_s + \overline{S_{xMICRO}} + \overline{S_x}DD \tag{6}$$

On days where the temperature is below freezing and the wind speed (ws) is above a threshold T_{ws} set to 5 m s^{-1} (McClung & Schaerer 2006), the wind redistributed snowfall P_{wd} is:

$$P_{wd}(x_i, y_i) = \begin{cases} A_f \cdot \sum_{P_{z_{min}}}^{P_{z_{max}}} [P_z(x_i, y_i)] & \texttt{if } ws > T_{ws} \\ P_z(x_i, y_i) & \texttt{otherwise} \end{cases} \tag{7}$$

It should be noted here that the threshold wind speed is applied to a single wind speed value measured at the Tarfala AWS. Such a measure is far from representative from wind speeds on Storglaciären and its surrounding ridges, which generally undergo local topographically and thermally driven wind fields (Lewis et al. 2008; Eriksson 2014). Nevertheless, the threshold value can be considered as a scaled indication of windiness in the area.

The difference between wind redistributed snowfall and the original elevation corrected snowfall is the net contribution from snow drift. Wind transported snow has generally high densities, as crystals get broken up during collisions with each other and the surface, decreasing the grain specific surface area and thus reducing pore space once the snow is deposited (e.g. Sato et al. 2008). In the EBFM snow model, this process is included in the description of fresh snow density as a function of wind speed and temperature, as given by Kampenhout et al. (2017). The same description is applied to the wind drifted snow.

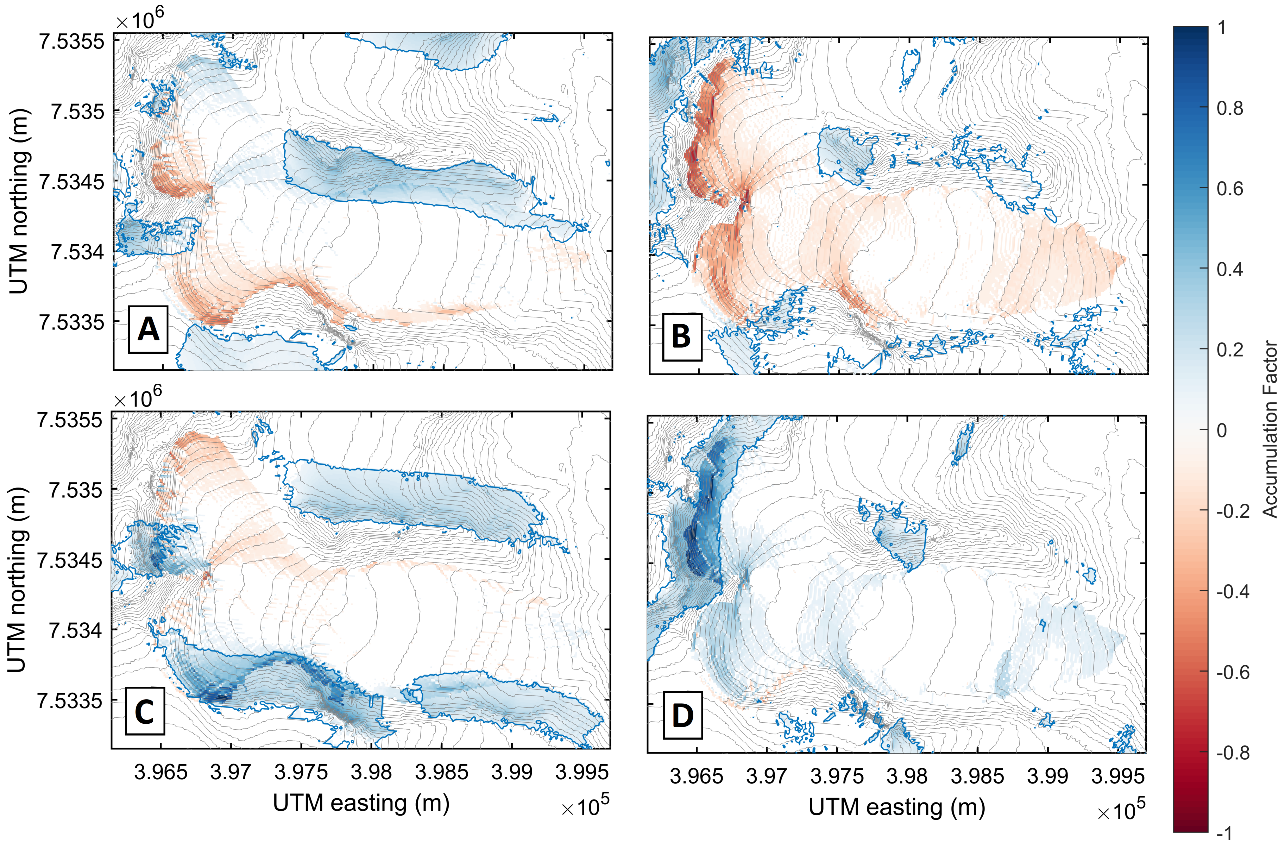

Figure 8: Accumulation Factor A_f for $SD_{max} = 330$ metres, shown for the four cardinal wind directions. A positive accumulation factor indicates and area prone to accumulation under the wind direction, while a negative accumulation factor indicates an area prone to erosion. Blue contour indicates the edges of the zones in the lee of major slope breaks. Accumulation within these zones is driven by larger scale wind effects($\overline{S_x}$), while accumulation and erosion outside of them is linked to micro scale snow drift ($\overline{S_{xMICRO}}$). **A** sheltering from northerly wind; **B** sheltering from easterly wind; **C** sheltering from southerly wind; **D** sheltering from westerly wind. Underlying topography is the Storglaciären catchment basin, with a contour interval of 20 metres.

S.5: Gravitational Snow Transport Model Description

The angle of repose of snow grains depends on several components, including the snow liquid water content and grain type, as well as the roughness and temperature of the surface it is deposited on (e.g. Willibald et al. 2020). Nevertheless, the net amount of deposited snow retained by a steep mountain side remains principally driven by the slope angle (Sommer et al. 2015). Following Gruber (2007), the maximum amount of snow D_{max} that can be retained by any cell follows a linear relationship driven by the slope angle β:

$$D_{max} = \begin{cases} (1 - \frac{\beta}{\beta_{lim}}) \cdot D_{lim} & \texttt{if } \beta < \beta_{lim} \\ 0 & \texttt{if } \beta \geq \beta_{lim} \end{cases} \tag{8}$$

Here, D_{lim} is the maximum amount of snow that is retained by a flat surface. β_{lim} is the steepest slope that retains any snow. The angle of repose of dry snow grains varies between 20° and 45° with grain type and temperature, and evolves further with metamorphism in the snowpack (Abe 2004; Willibald et al. 2020). This complexity is increased further in the consideration of topography with non-uniform slope angles and variable temperature, humidity and wind speed (Sommer et al. 2015). The diversity in snow retainment is illustrated by examples of vertical faces holding rime, while slopes below 20° can produce glide snow avalanches (McClung & Schaerer 2006). Nevertheless, observations show that snow mass deposited in terrain above a certain steepness is likely to undergo gravitational transport rather than melt in place (Bl & Kirnbauer 1992; Kerr et al. 2013). Here, β_{lim} is an estimation of this steepness, and can be calibrated as a model parameter. D_{max} governs the maximum deposit thickness that can be attained before the inflow of snow is transferred to surrounding cells. D_{max} varies between D_{lim} at $\beta = 0$ and zero at $\beta = \beta_{lim}$. D_{lim} also regulates the avalanche extent: a lower maximum deposition at low slope angles will result in spread out and shallow deposits. The Gruber (2007) routine does not include any limitation other than a zero slope on the maximum distance the deposit can reach. This has little consequences on the description of relatively simple two part terrain forms that consist of a steep headwall and a flat runout area. However, it can lead to erroneous gravitational transport on terrain that has slope angles above 0° but well below β_{lim} on time-steps of high snowfall, where the precipitation exceeds D_{max}. Although maximum runout distance reached by deposits of snow avalanches depends on the moving mass, snow conditions, and a vast array of terrain characteristics (e.g. Christen et al. 2010), estimation of the maximum "reach" of an avalanche based on terrain only is a common necessity in snow hazard assessment. Lied & Bakkehøi (1980) propose an empirical relation between a set of terrain based parameters and the smallest runout angle α_{min} between the horizontal plane and the avalanche starting zone. The furthest distance reached by avalanching snow then corresponds to α_{min}, meaning that any point x along the avalanche path with an angle to the starting zone $\alpha_x > \alpha_{min}$ falls within the deposition zone, while any point with $\alpha_x < \alpha_{min}$ will not be reached by avalanching snow (Fig. 9). Lied & Bakkehøi (1980) derive the α_{min} from observations on a set of avalanche paths in Norway, finding that 99.8% of avalanches to stay within an α angle of 18°, while 75% of avalanches stay within $\alpha = 27°$. These statistical estimations of runout distances are widely used in terrain based snow hazard mapping (Larsen et al. 2020) and can be utilized along the gravitational transport model to confine the mass deposition in space.

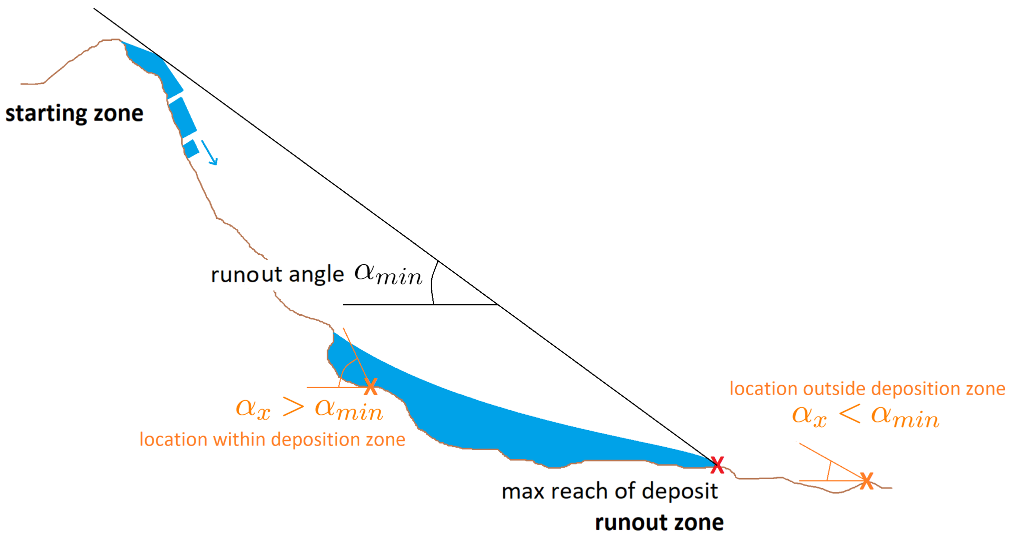

Figure 9: **Based on Lied & Bakkehøi (1980).** Delimitation of terrain subject to be reached by avalanche deposits.

For each gridcell, "slices" of 30° are considered in each cardinal direction, in an approach that is identical to the sheltering index estimation in section S.4. α is estimated by using equation 1, indicating the angle to the highest point of the topography in each direction. A maximum scanning distance of 1000 m is used to ensure all terrain is considered without including topography outside the catchment. For each grid-cell, the highest α of the four considered directions is retained:

$$\alpha(x,y) = \max(\alpha_N(x,y),\ \alpha_E(x,y),\ \alpha_S(x,y),\ \alpha_W(x,y)) \tag{9}$$

D_{max} is then adjusted following a comparison between α and α_{min} (Fig. 10):

$$D_{max} = \begin{cases} (1 - \frac{\beta}{\beta_{lim}}) \cdot D_{lim} & \texttt{if } \beta < \beta_{lim} \ \texttt{\&} \ \alpha > \alpha_{min} \\ 0 & \texttt{if } \beta \geq \beta_{lim} \ \texttt{\&} \ \alpha \leq \alpha_{min} \end{cases} \tag{10}$$

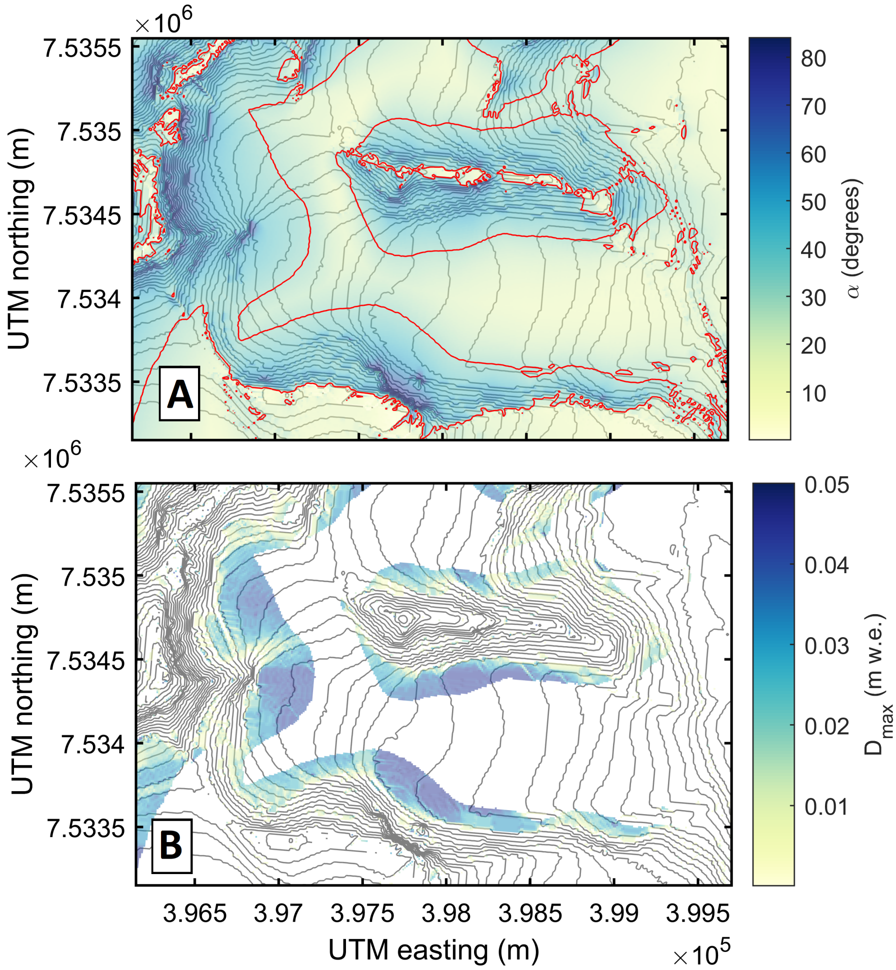

Figure 10: **A** α angle to highest surrounding terrain. Red contour indicates $\alpha = 30°$, the maximum reach of approximately 75% of avalanches. **B** Maximum deposit thickness D_{max}. D_{max} is zero where the terrain is steeper than β_{lim} and when α is below α_{min}. Underlying topography is the Storglaciären catchment basin, 20 m contours.

If for any cell the amount of mobile mass M constitutes of the snow mass in the cell and any additional precipitation I:

$$M = M_{initial} + I \tag{11}$$

The deposition in a cell is equal to either the amount of mobile mass M it contains, or to its maximum snow holding capacity D_{max} if the latter is exceeded by M.

$$D = \begin{cases} M & \texttt{if } M < D_{max} \\ D_{max} & \texttt{if } M \geq D_{max} \end{cases} \tag{12}$$

The excess of mass is then available for avalanching and gets redistributed to surrounding cells:

$$F_n = (M - D) \cdot f_n \tag{13}$$

Where F_n is the amount of mass going to a neighbouring cell n, while f_n is the fraction of the available mass that is allocated to the neighbouring cell n (eq.17, which depends on terrain parameters. Following Gruber (2007), the lateral transfers between any cell and its four cardinal neighbours are considered. The share of material that is transferred to each cell depends on the aspect of the slope that contains the cells. In the fall line, the length of the opening L_n toward the four cardinal surrounding cells then follows, where α is the aspect angle and Cs is the individual cell width:

$$\begin{aligned}L_1 &= cos(\alpha) \cdot Cs \\ L_2 &= -sin(\alpha) \cdot Cs \\ L_3 &= sin(\alpha) \cdot Cs \\ L_4 &= -cos(\alpha) \cdot Cs\end{aligned} \tag{14}$$

As only uphill flow should be considered, a conditional parameter is established using Δ_z the elevation difference to neighbouring cells:

$$Ho = \begin{cases} 1 & \texttt{if } \Delta_z > 0 \\ 0 & \texttt{if } \Delta_z \leq 0 \end{cases} \tag{15}$$

The condition is used to correct the flow width L_n so that no uphill flow can occur:

$$CL_n = Ho \cdot \Delta_z \cdot L_n \tag{16}$$

As in Gruber (2007), the obtained parameter is normalized in order to obtain the fragmentation of the transferred mass over the four cardinal surrounding cells:

$$f_n = \frac{CL_n}{CL_1 + CL_2 + CL_3 + CL_4} \tag{17}$$

The fractions of mass transfer f_n in the four cardinal directions are converted to four mass transfer volumes F_nN, F_nW, F_nE and F_nS following equation 13, allowing for the adjustment of the mass M present in each of the four cardinal surrounding cells:

$$\begin{aligned}M(x,y-1) &= M(x,y-1) + F_nN(x,y) \\ M(x-1,y) &= M(x-1,y) + F_nW(x,y) \\ M(x+1,y) &= M(x+1,y) + F_nE(x,y) \\ M(x,y+1) &= M(x,y+1) + F_nS(x,y)\end{aligned} \tag{18}$$

Within a time-step, all cells are treated in order of maximum to minimum elevation, to ensure each cell has received all mass before transfer away from it is considered. Finally, the coupling of gravitational mass transport to mass balance requires a time step specific output of newly deposited mass onto the glacier surface. The precipitation is subtracted from the deposition value to prevent it being counted double:

$$\delta D_t(x,y) = D_t(x,y) - I_t(x,y) \tag{19}$$

Mass deposited by avalanches enters the snow model routine with specific characteristics. From a series of lab experiments, Maeno et al. (1987) describe the density of dry snow avalanche deposits to vary between 450 kg m^{-3} and 600 kg m^{-3}. The estimate varies with the avalanche's flow rate and density, as well the snow's initial water content (McClung & Schaerer 2006). Here the initial density of avalanched mass is set to 500 kg m^{-3}.

Avalanches deposits have a different surface roughness than snow cover resulting from precipitation, and thus carry different radiative properties. However, the reflectance of solar radiation by avalanche deposits depends on the illumination angle, meaning that the broadband albedo is not straightforward to estimate (Bühler et al. 2009; Treichler et al. 2009). In addition, debris from large avalanches can contain high percentages of impurities, which significantly reduces the broadband albedo (Scally 1992). The phenomenon is very event dependent and thus difficult to constrain: as a result, no distinction in albedo is made here between avalanche deposits and precipitated snow cover.

Finally, the temperature of avalanche deposits is governed by the average snow temperature of the initially released layers, the temperature of entrained snow, latent heat fluxes driven by phase changes and kinetic energy dissipation from shearing within the avalanche (Vera Valero et al. 2015). Temperature increases driven by kinetic energy dissipation can warm the deposit by several degrees relative to surrounding snow, meaning they should be taken into consideration when calculating the surface energy balance and snow conditions. A relatively simple approach is proposed by Steinkogler et al. (2015): latent heat dissipation is left out of consideration under the assumption that the snow remains entirely dry throughout transport, and all potential energy is assumed to be transformed to heat. The friction driven temperature increase then follows:

$$\Delta T_{friction} = \frac{m \cdot g \cdot \Delta H}{m \cdot c_p} \tag{20}$$

where the moving mass m cancels out, the gravitational acceleration constant $g = 9.8\ m\ s^{-1}$, the specific heat capacity of snow $c_p = 2116\ J\ kg^{-1}\ K^{-1}$ and ΔH is the elevation difference between the onset of movement and the deposition location. As a large share of the deposited mass during an avalanche does not come from the initial release zone but has been entrained along the path and thus would have undergone a shorter vertical drop, Steinkogler et al. (2015) propose a formulation of ΔH that assumes entrainment occurs evenly along the avalanche path:

$$\Delta H = \frac{\Delta h_r \cdot (m_r + 0.5 m_e)}{m_r + m_e} \tag{21}$$

Δh_r is the elevation difference to the initial release zone. The value is computed for each gridcell to estimate the maximum angle to surrounding start zones (Fig. 9; eq.9), and can thus be re-employed here. Within the Gruber (2007) model, the initially released mass m_r is assumed to be equal to the incoming precipitation of the deposit cell. This is a simplification as it assumes constant precipitation across the grid (negating wind and elevation driven precipitation increases) and introduces slight error in the rare event that the initial release occurs in a cell where $D_{max} > 0$ and reaches its threshold at the deposition producing time step. The entrained mass m_e is the difference between the deposited mass and the initially released mass. The assumption that entrainment occurs evenly along the path is again a slight simplification here, as it fails to account for precipitation variability and reduced entrainment in the deposition zone. The resulting temperature change ΔT is added to the original surface temperature of the gridcell in which deposition occurs, under an additional assumption that surface temperature is constant across the entire avalanche path.

S.6: Detail of spatially distributed model error

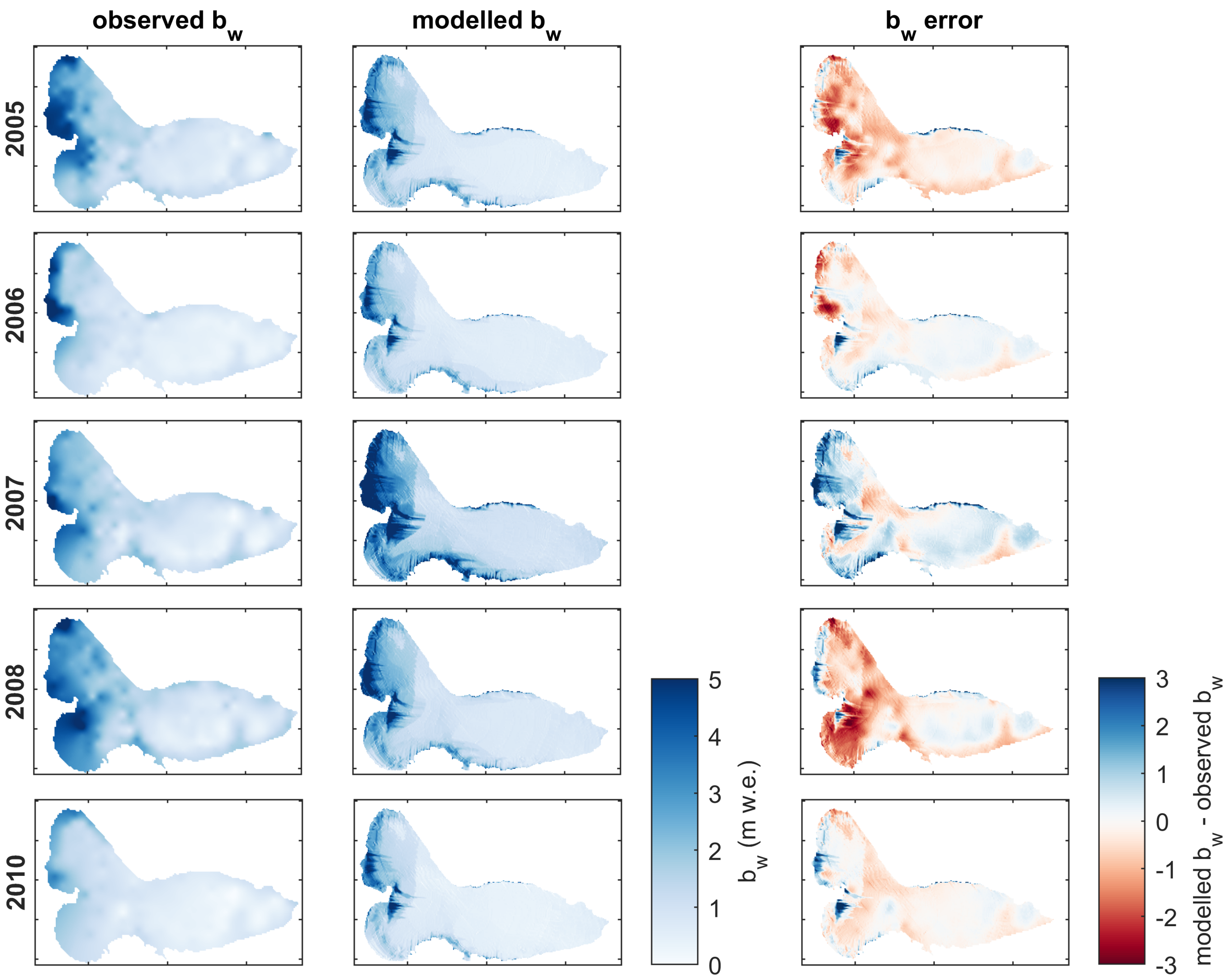

Figure 11: Comparison of observed and modelled winter balance for each accumulation season of the validation period. **A** Observed winter balance, interpolated from probe network measurements. **B** Winter balance modelled with ST-EBFM. **C** Error on ST-EBFM b_w. The error is negative when the model underestimates b_w and positive when the model overestimates b_w.

References

Abe O. (2004). Shear strength and angle of repose of snow layers including graupel. *Annals of Glaciology* 38, pp. 305–308. DOI: 10.3189/172756404781815149.

Bl G. ö. & Kirnbauer R (1992). An analysis of snow cover patterns in a small alpine catchment. *Hydrological Processes* 6.1, pp. 99–109. DOI: 10.1002/hyp.3360060109.

Bühler Y, Hüni A, Kellenberger T., & Itten K. (2009). Towards an automated detection of avalanche deposits using their directional properties. DOI: 10.5167/uzh-18485.

Christen M., Kowalski J., & Bartelt P. (2010). RAMMS: Numerical simulation of dense snow avalanches in three-dimensional terrain. *Cold Regions Science and Technology* 63.1-2, pp. 1–14. DOI: 10.1016/j.coldregions.2010.04.005.

Eriksson P. (2014). Meteorological differences between Rabots glaciär and Storglaciären and its impact on ablation. MA thesis.

Evans E., Essery R., & Lucas R. (2008). Changing snow cover and the net mass balance of Storglaciären, northern Sweden. *Annals of Glaciology* 49, pp. 199–204. DOI: 10.3189/172756408787814933.

Gruber S. (2007). A mass-conserving fast algorithm to parameterize gravitational transport and deposition using digital elevation models. *Water Resources Research* 43.6. DOI: 10.1029/2006WR004868.

Jansson P., Linderholm H. W., Pettersson R., Karlin T., & Mörth C.-M. (2007). Assessing the possibility to couple the chemical signal in winter snow on Storglaciären, Sweden, to atmospheric climatology. *Annals of Glaciology* 46, pp. 335–341. DOI: 10.3189/172756407782871459.

Jansson P. & Pettersson R. (2007). Spatial and Temporal Characteristics of a Long Mass Balance Record, Storglaciären, Sweden. *Arctic, Antarctic, and Alpine Research* 39.3, pp. 432–437. DOI: 10.1657/1523-0430(06-041)[JANSSON]2.0.CO;2.

Kampenhout L. van, Lenaerts J. T., Lipscomb W. H., Sacks W. J., Lawrence D. M., Slater A. G., & Broeke M. R. van den (2017). Improving the representation of polar snow and firn in the Community Earth System Model. *Journal of Advances in Modeling Earth Systems* 9.7, pp. 2583–2600. DOI: 10.1002/2017MS000988.

Kerr T., Clark M., Hendrikx J., & Anderson B. (2013). Snow distribution in a steep mid-latitude alpine catchment. *Advances in Water Resources* 55, pp. 17–24. DOI: 10.1016/j.advwatres.2012.12.010.

Larsen H. T., Hendrikx J., Slåtten M. S., & Engeset R. V. (2020). Developing nationwide avalanche terrain maps for Norway. *Natural Hazards* 103.3, pp. 2829–2847. DOI: 10.1007/s11069-020-04104-7.

Lewis H., Mobbs S., & Lehning M (2008). Observations of cross-ridge flows across steep terrain. *Quarterly Journal of the Royal Meteorological Society: A journal of the atmospheric sciences, applied meteorology and physical oceanography* 134.633, pp. 801–816. DOI: 10.1002/qj.259.

Lied K. & Bakkehøi K (1980). Empirical calculations of snow–avalanche run–out distance based on topographic parameters. *Journal of Glaciology* 26.94, pp. 165–177. DOI: 10.3189/S0022143000010704.

Maeno N, Naruse R, & Nishimura K (1987). Physical characteristics of snow-avalanche debris (Davos, Switzerland). Vol. 162. IAHS Publ, pp. 421–427.

McClung D. & Schaerer P. A. (2006). *The Avalanche Handbook*. The Mountaineers Books. ISBN: 978-0-89886-809-8.

McGrath D., Sass L., O'Neel S., McNeil C., Candela S. G., Baker E. H., & Marshall H.-P. (2018). Interannual snow accumulation variability on glaciers derived from repeat, spatially extensive ground-penetrating radar surveys. *The Cryosphere* 12.11, pp. 3617–3633. DOI: 10.5194/tc-12-3617-2018.

Sato T., Kosugi K., Mochizuki S., & Nemoto M. (2008). Wind speed dependences of fracture and accumulation of snowflakes on snow surface. *Cold Regions Science and Technology* 51.2-3, pp. 229–239. DOI: 10.1016/j.coldregions.2007.05.004.

Scally F. A. de (1992). Influence of avalanche snow transport on snowmelt runoff. *Journal of Hydrology* 137.1-4, pp. 73–97. DOI: 10.1016/0022-1694(92)90049-2.

Schweizer J., Bruce Jamieson J, & Schneebeli M. (2003). Snow avalanche formation. *Reviews of Geophysics* 41.4. DOI: 10.1029/2002RG000123.

Sommer C. G., Lehning M., & Mott R. (2015). Snow in a very steep rock face: Accumulation and redistribution during and after a snowfall event. *Frontiers in Earth Science* 3, p. 73. DOI: 10.3389/feart.2015.00073.

Steinkogler W., Sovilla B., & Lehning M. (2015). Thermal energy in dry snow avalanches. *The Cryosphere* 9.5, pp. 1819–1830. DOI: 10.5194/tc-9-1819-2015.

Treichler D, Bühler Y, Hüni A, Kneubühler M, & Itten K. (2009). Spectral Discrimination of Avalanche Deposits. *6th EARSeL SIG Workshop: Imaging Spectroscopy, Tel Aviv, Israel.*

Vera Valero C., Jones K. W., Bühler Y., & Bartelt P. (2015). Release temperature, snow-cover entrainment and the thermal flow regime of snow avalanches. *Journal of Glaciology* 61.225, pp. 173–184. DOI: 10.3189/2015JoG14J117.

Willibald C., Löwe H., Theile T., Dual J., & Schneebeli M. (2020). Angle of repose experiments with snow: role of grain shape and cohesion. *Journal of Glaciology* 66.258, pp. 658–666. DOI: 10.1017/jog.2020.36.

Winstral A., Elder K., & Davis R. E. (2002). Spatial snow modeling of wind-redistributed snow using terrain-based parameters. *Journal of Hydrometeorology* 3.5, pp. 524–538. URL: http://www.jstor.org/stable/24909301.